Available online at www.sciencedirect.com
SCIENCE DIRECT®
Journal of Nuclear Materials 348 (2006) 263–271
journal of nuclear materials
www.elsevier.com/locate/jnucmat

The effect of grain boundary engineering on the oxidation behavior of INCOLOY alloy 800H in supercritical water

L. Tan, K. Sridharan, T.R. Allen *

Department of Engineering Physics, University of Wisconsin–Madison, 1500 Engineering Drive, Madison, WI 53706, USA

Received 31 March 2005; accepted 27 September 2005

Abstract

Grain boundary engineering (GBE) was applied to INCOLOY alloy 800H by means of thermomechanical processing. The oxidation behavior of GBE-treated alloy 800H exposed in supercritical water (SCW) with 25 ppb dissolved oxygen at 500 °C and 25 MPa was significantly improved as compared to 800H in the annealed condition. Gravimetry, optical microscopy, scanning electron microscopy/energy dispersive X-ray spectroscopy (SEM/EDS), X-ray diffraction (XRD), and electron backscatter diffraction (EBSD) were employed in this study to analyze the oxidation behavior of control (annealed) and GBE-treated samples. GBE improves the protective oxidation behavior by enhancing spallation resistance and reducing oxidation rate. Spallation resistance correlates with a reduction in texture of the oxide layers.

PACS: 81.65.Mq; 81.40.Gh; 61.14.−x; 61.82.Bg

1. Introduction

Grain boundary engineering (GBE), proposed by Watanabe [1] in the early 1980s, has been found to promote a high proportion of low-Σ ($\Sigma \leqslant 29$) coincidence site lattice (CSL) boundaries (CSLBs) in materials. GBE has been extensively investigated as an approach to improve properties such as strength [2], creep [3], and intergranular corrosion or stress corrosion resistance [4]. In the CSL model, the newly formed superlattice is denoted by Σ, where the Σ value is defined as the reciprocal of the fraction of lattice points that coincide between the two adjoining grains across the boundaries. The low-Σ CSLBs contain more coincident lattice points across the grain boundaries. Thus, there is a low distortion of atomic bonds and relatively small free volume for CSLBs and consequently low boundary energy. Among the low-Σ CSLBs, the contribution of $\Sigma 3$ to property improvement is the most prevalent [1,5,6]. This is because the energy of $\Sigma 3$ boundaries is extremely low, typically about 1/50 of a general boundary [7]. Detailed information about the CSL model and CSL effect on GBE can be found in Ref. [7].

* Corresponding author. Tel.: +1 608 265 4083; fax: +1 608 263 7451.
E-mail address: allen@engr.wisc.edu (T.R. Allen).

0022-3115/$ - see front matter © 2005 Elsevier B.V. All rights reserved.
doi:10.1016/j.jnucmat.2005.09.023

Since its introduction to the market in the 1950s, INCOLOY alloy 800H (UNS N08810) has been broadly utilized in furnace components and equipment, petrochemical furnace cracker tubes, pigtails and headers, and sheathing for electrical heating elements. Based on its advantages such as high strength and corrosion resistance at high temperatures, alloy 800H was selected as one of the potential candidate alloys for Generation IV supercritical water-cooled nuclear plant designs [8]. Alloy 800H is an austenitic solid–solution alloy with iron (~45 wt%), nickel (~31 wt%) and chromium (~20 wt%) as major constituent elements. It is generally used in the annealed condition, with a microstructure consisting of the matrix austenite phase and small amounts of precipitates such as titanium nitrides, titanium carbides, and chromium carbides. Alloy 800H has excellent resistance to oxidation due to its high chromium and nickel contents. The chromium in this alloy promotes the formation of a protective surface oxide, and the nickel enhances the stability of the protective oxide, especially during cyclic exposure to high temperatures [9]. Otsuka and Fujikawa [10] studied the oxidation behavior of alloy 800H exposed in high-temperature steam at 700 °C, and found that a uniform duplex thin oxide scale formed on this alloy. The outer oxide layer is composed of Fe_3O_4 with some Fe_2O_3, and the inner oxide layer is primarily $(Fe,Cr)_3O_4$ spinel. In addition, trace amounts of oxides, probably Cr_2O_3 or Al_2O_3, were observed dispersed within the metal substrate ahead of the inward-growing inner spinel [10,11].

Supercritical water (SCW), with temperature and pressure above the critical point of water at 374 °C and 22.1 MPa, has been employed in modern fossil power plants to improve thermal efficiency and reduce the release of deleterious gases such as carbon dioxide, nitrogen oxides and sulfur oxides. Because of the potential for increased thermal efficiency, SCW has also been proposed as a coolant for Generation IV nuclear plants [8]. Limited literature exists on the oxidation behavior of alloy 800H exposed in supercritical water (SCW). Preliminary results of SCW-exposed alloy 800H at 500 °C and 25 MPa indicates that severe spallation occurred after ~333 h exposure [12]. Because spallation of the oxide scale may cause blockage inside superheater/reheater tubes [13] or a severe erosion damage at turbine blades, information about scaling behavior of alloy 800H is needed. To withstand an aggressive environment with high-temperature and pressure in modern and future power plant system, the properties of alloy 800H are desired to be improved for extended service lifetime and system stability.

Grain boundary character distribution in alloy 800H was tuned by means of thermomechanical processing to improve the stability of the thermally-grown external oxide scale. This paper presents the effect of GBE on oxidation of alloy 800H by comparing control (annealed) and GBE-treated samples. Gravimetry, optical microscopy, scanning electron microscopy/energy dispersion X-ray spectroscopy (SEM/EDS), X-ray diffraction (XRD), and electron backscatter diffraction (EBSD) were used to analyze oxide growth and stability.

2. Experiment

The material used in this study was commercial INCOLOY alloy 800H with the measured chemical composition (in wt%): 45.26 Fe, 31.59 Ni, 20.42 Cr, 0.76 Mn, 0.57 Ti, 0.50 Al, 0.42 Cu, 0.13 Si, 0.069 C, 0.014 P, and 0.001 S. Rectangular samples (31.7 × 12.7 mm) with a thickness of ~1 mm were cut from the as-received alloy that had been annealed at 1177 °C for 24 min/cm of thickness followed by water quench. Some of the rectangular samples were subjected to a cold rolling with a thickness reduction of ~7% followed by annealing at 1050 °C for 90 min. This thermomechanical processing, straining followed by annealing, has been successfully used to increase the population of low-Σ CSLBs in our previous work [14] while maintaining the minimum grain size requirement of alloy 800H, ~60 μm [9]. The control (cut from annealed material) and GBE-treated (thermomechanical-processed) samples were polished to 1 μm finish prior to exposure in SCW with 25 ppb (part per billion) dissolved oxygen at conditions of 500 °C and 25 MPa for exposure times to 1026 h. The oxidation behavior of these samples was analyzed in this work by means of gravimetry, optical microscopy, SEM/EDS, XRD, and EBSD.

A LEO 1530 field emission gun scanning electron microscope (FEGSEM) was employed for SEM/EDS analyses. Secondary electron image (SEI) mode was employed to study surface morphology in plan-view and oxide scale structure in cross-section. To obtain good quality EBSD patterns, the cross-section samples were ground with SiC abrasive paper up to 1200 grit followed by polishing with diamond paste, alpha alumina and colloidal

silica solutions in sequence. The EBSD investigation was performed in a LEO 1530 FEGSEM incorporated with the TSL orientation imaging microscopy (OIM) system MSC2200. The SEM was operated at 20 kV, and the automatic EBSD area scan was performed using a hexagonal grid with a step size of 0.1 μm. To allow identification of the existing phases with the EBSD analytical software, crystallographic data files were established based on the XRD analysis performed in this work together with the available database included in the OIM software. For phase analysis with EBSD, a voting scheme and the confidence index (CI) established by TSL were used [15]. A high number of votes and high CI values indicate that the phase is correctly identified with a high probability.

3. Results and discussion

3.1. CSLBs of control and GBE-treated samples

The frequency of low-Σ CSLBs in the control and GBE-treated samples was analyzed by means of EBSD and is shown in Fig. 1. Similar frequencies of $\Sigma 1$ and $\Sigma 3$ were observed in the control sample. The $\Sigma 1$ frequency could be introduced into the system by texture, the presence of many sub-boundaries in the material, and recombination of two like boundaries impinging on each other. Generally, the reported total frequency of low-Σ CSLBs does not include the contribution from $\Sigma 1$ due to ambiguities in distinguishing these interfaces from sub-boundaries present in materials. The $\Sigma 3$ frequency of the GBE-treated sample was promoted to 59% from 36% in the control sample. Meanwhile, the $\Sigma 3^n$ ($\Sigma 9$ and $\Sigma 27$) frequencies also were increased compared to the control sample. According to the results of the EBSD analysis, the total frequency of low-Σ CSLBs was greatly increased by thermo-mechanical processing.

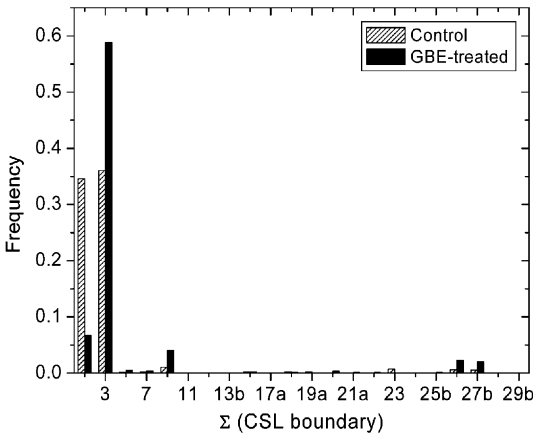

Fig. 1. CSL frequency as a function of low-Σ CSLBs ($\Sigma \leqslant 29b$) of control and GBE-treated samples.

3.2. Gravimetry

The weight gain of control and GBE-treated samples after SCW exposure is plotted in Fig. 2. The dashed and solid curves indicate the trend of the weight gain as a function of exposure time for control and GBE-treated samples, respectively. The weight gain data of the control samples has large fluctuations. Weight gain increased initially with short-time SCW exposure. After an ~2-week SCW exposure, sudden weight loss occurred on the control samples, which may result from oxide spallation as discussed later. In contrast, the weight gain of GBE-treated samples gradually increased due to oxide growth during SCW exposure time up to ~4-weeks and then mildly decreased due to the possible occurrence of minor oxide spallation. Although the weight gain data of the GBE-treated samples are limited compared to those of the control samples, their difference, especially after ~4-week SCW exposure, is significant. Therefore,

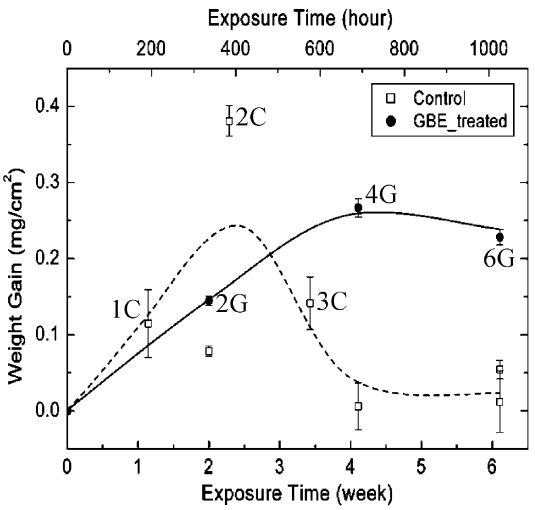

Fig. 2. Weight gain of SCW-exposed control and GBE-treated alloy 800H samples. The error bars indicate the propagated error for the measurements of weight and exposure area. The dashed and solid curves indicate the trend of the weight gain change over exposure time for control and GBE-treated samples, respectively. The labels, XC and XG, denote approximate weeks of exposure time (X) for control (C) and GBE-treated (G) samples.

optical microscopy, SEM/EDS, and EBSD were utilized to analyze the difference in the oxides formed on the control and GBE-treated samples. Three typical control samples, 1C, 2C and 3C where the numbers and C denote the approximate SCW exposure time in weeks and control samples (e.g. 3C is a control sample exposed for ~3 weeks), were chosen to be analyzed due to their representative oxide thickness change. GBE-treated samples, 2G, 4G and 6G, where the numbers and G denote the approximate SCW exposure time in weeks and GBE-treated samples, were analyzed to compare them with control samples.

3.3. Oxide morphology

Oxide morphologies, analyzed with optical microscopy and SEM, are shown in Fig. 3 with the optical image on the left and corresponding secondary electron image (SEI) on the right for each sample. The low magnification optical images indicate that a continuous layer of oxide with distinct grain contrast formed on short-time SCW-exposed samples such as 1C and 2G. Oxide spallation occurred after ~2-week SCW exposure for the control samples as shown in Fig. 3 (2C sample), and the spallation area increased with longer exposure time as shown in the 3C sample. The extensive oxide spallation resulted in the weight loss of the control samples after ~2-week SCW exposure as shown in Fig. 2. In contrast, no obvious spallation was observed in the optical images of GBE-treated samples with up to ~6-week exposure time. Another observed phenomenon in the optical images is that the grain contrast of the oxide dims with exposure time for both control and GBE-treated samples. The grain contrast change can be explained from the corresponding high magnification SEIs as shown in Fig. 3. The oxide of the short-time SCW-exposed samples such as 1C and 2G showed distinct facets that may effectively influence light reflection strength giving distinct contrast. With the increase of SCW exposure time, the oxide topography changed to serration (2C sample) and discrete oxide islands (3C sample) on the control samples, and mild undulation (4G and 6G samples) on the GBE-treated samples. The serration, discreteness, and undulation of the oxide may diminish the difference in light reflection and thus cause the reduction of contrast.

3.4. Oxide layer structure

Oxide layer structure is presented in SEIs of cross-section specimens of control and GBE-treated samples. As shown in Fig. 4, the oxide on both control and GBE-treated samples had a dual-layer structure. The oxide layer on all samples was

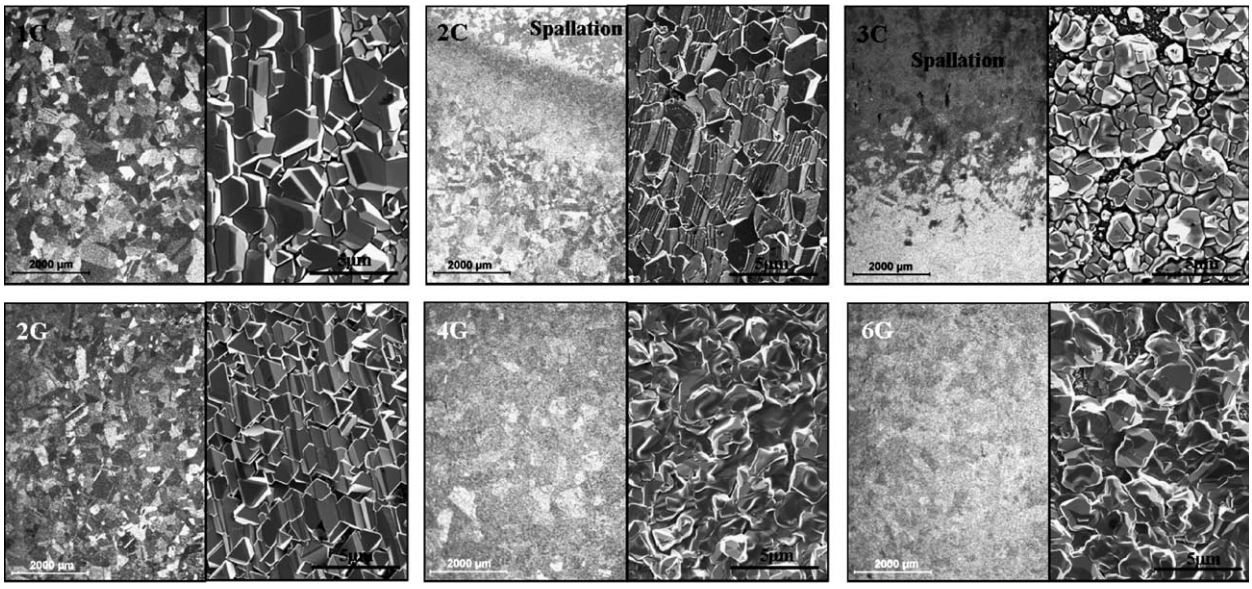

Fig. 3. Low-magnification optical images (left) and corresponding high-magnification SEM images (right) of each sample (1C, 2C, 3C, 2G, 4G and 6G) indicate the oxide morphology of SCW-exposed control (C) and GBE-treated (G) samples.

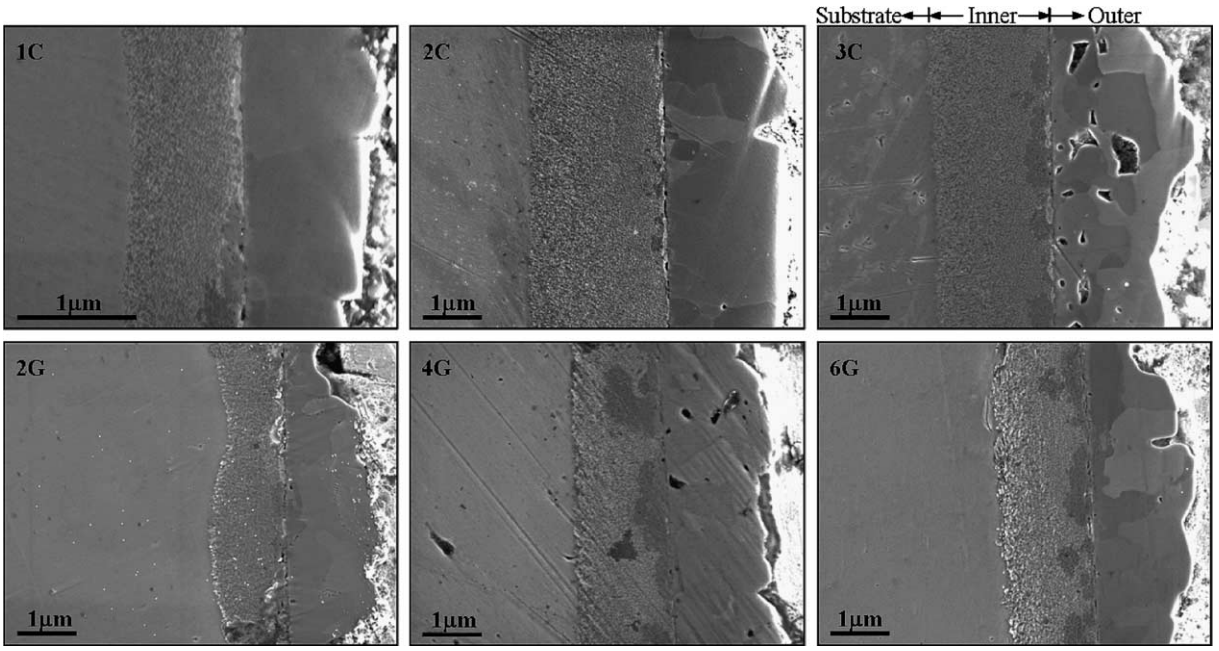

Fig. 4. Cross-section secondary electron images (SEIs) representing well maintained oxide scale formed on control (1C, 2C and 3C) and GBE-treated (2G, 4G and 6G) samples indicating a dual-layer oxide scale formed on the metal substrate.

compact without evident pores except for long-time SCW-exposed control samples, such as sample 3C. This compact oxide structure is generally not observed in oxide formed on ferritic/martensitic alloys [16]. The interface between the outer and the inner oxide layers of the GBE-treated samples was not as sharp as that of the control samples. The SEIs in Fig. 4 indicate that more intermixing has occurred at the interface between the outer and the inner oxide layers on the GBE-treated samples than that which occurs on the control samples. The increased intermixing that occurred at the interface on the GBE-treated samples may contribute to stronger adhesion between the outer and the inner oxide layers and thus alleviate oxide spallation.

Due to the extensive oxide spallation and the difficulty in maintaining the fairly thin oxide scale during cross-section SEM specimen preparation, the oxide scale thickness measured from SEIs is not reliable. Since the oxide scale growth rate (or oxidation rate) of the alloy is strongly affected by the inner oxide layer [13,17], oxide scale was evaluated by the thickness of the inner oxide layer. As shown in Fig. 4, the thickness of the inner oxide layer of the GBE-treated samples is similar to or thinner than that of the control samples even though the SCW exposure time of the GBE-treated samples was about twice that of the control samples. The thinner inner oxide layer indicates that GBE-treated samples experienced a slower oxidation rate than control samples. Other oxides reported in the literature [10,11] such as Cr_2O_3 and Al_2O_3 were not observed in this study.

To further study the oxidation behavior difference between control and GBE-treated samples in terms of composition, crystal structure and texture, EDS and EBSD were employed. Samples 3C and 4G are used as examples here to illustrate the oxidation behavior of control and GBE-treated samples, respectively, because they have thick enough oxides to be analyzed and similar SCW exposure times. The EDS line-scan data along the cross-section of the 3C and 4G samples are plotted in Fig. 5. The major components (O, Fe, Ni and Cr) and minor components (Al, Si and Ti) showed similar distributions in the oxide scale on the control and GBE-treated samples. As shown in Fig. 5, Fe was depleted in the inner oxide layer and enriched in the outer oxide layer. Ni and Cr were maintained in the inner oxide layer and depleted in the outer oxide layer with a small Ni-enrichment at the interface of the metal substrate and the oxide layer. Thus, the outer and inner oxide layers consisted of Fe-dominated oxide and complex oxide, respectively.

For minor components, some Al and Si diffused into the outer oxide layer, while Ti was not observed

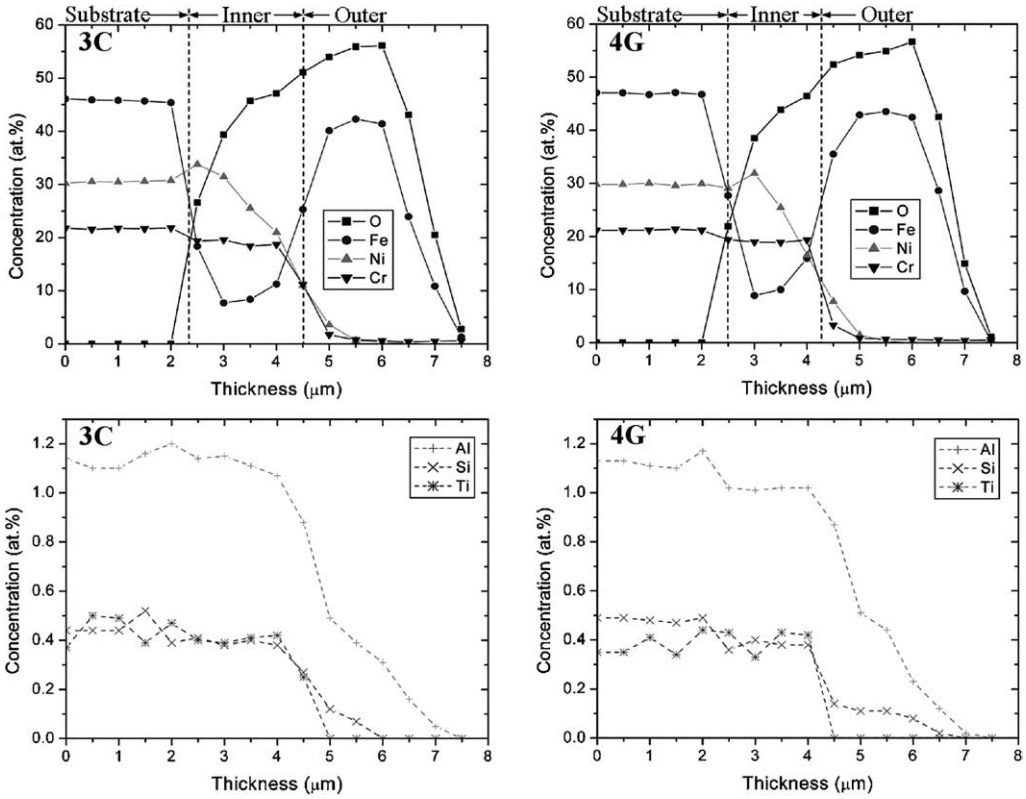

Fig. 5. EDS line-scan over cross-section of ~3-week SCW-exposed control (3C) and ~4-week SCW-exposed GBE-treated (4G) samples.

in the outer oxide layer. Even though the 3C and 4G samples displayed similar constituent distribution, the inner oxide layer of the 4G sample was thinner than that of the 3C sample, which is consistent with the cross-section SEI results shown in Fig. 4. Generally, the transport of diffusing species along grain boundaries is much faster than through the grains. Low energy boundaries reduce the magnitude of grain boundary phenomena such as diffusion and precipitation, because their atomic structure is highly regular and/or coherent as compared with random grain boundaries. Therefore, it would be expected that the transport of diffusing species such as Fe and O would be depressed in GBE-treated samples with increased population of low energy boundaries, which would result in a slower oxidation rate (or thinner inner oxide layer).

EBSD scanning maps of samples 3C and 4G are shown in Fig. 6(a) and (b), respectively. The crystal structures of substrate and oxide on the control and GBE-treated samples were identified as austenite, magnetite/spinel (Fe_3O_4 structure), and hematite (Fe_2O_3 structure). Magnetite and spinel are not differentiated in EBSD analysis for simplification due

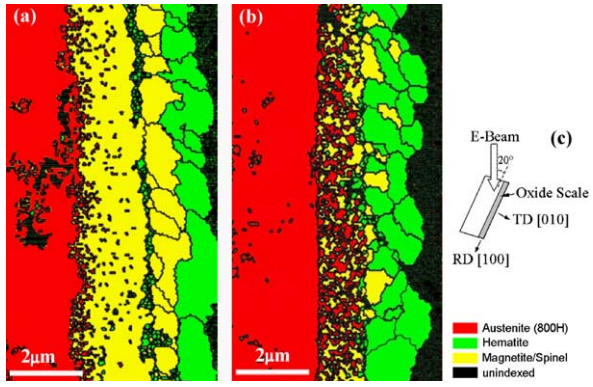

Fig. 6. EBSD scanning map of (a) 3-week SCW-exposed control (3C) and (b) 4-week SCW-exposed GBE-treated (4G) samples. The specimen layout during EBSD analysis is schematically shown in (c) with the direction of TD [0 1 0] and RD [1 0 0] parallel to oxide growth and oxide surface, respectively.

to their almost identical crystallographic structure. But they can be differentiated by the combination of the EBSD and EDS results. Unindexed areas are marked in black in Fig. 6. Some features in the substrate and oxide scale are unindexed, which

may be defects or minor phases not considered in this analysis. The phase distribution throughout the oxide layer structure is clearly presented in Fig. 6. The outer oxide layer is composed of hematite and magnetite. The inner oxide layer is a mixture of austenite (substrate) and spinel. The observed oxides, hematite, magnetite and spinel, were also confirmed by X-ray diffraction, the details of which are not included in this paper. The intermixing between austenite and spinel in the inner oxide layer on the 4G sample is stronger than that on the 3C sample, which increases the adhesion between substrate and oxide scale. It needs to be noted that the smaller observed intermixing between austenite and spinel observed in the inner oxide layer on the control sample as shown in Fig. 6(a) may also be due to the amount of austenite phase being less than the resolution limit of the EBSD technique. The formation of the fine intermixed structure in the inner oxide layer needs to be further investigated. In addition to the layer structure, Fig. 6 also shows information on phase fraction and oxide grain size. More hematite with relatively smaller grain size was formed on the 4G sample than that on 3C sample.

3.5. Oxide spallation

Gravimetry and optical topographical microscopy results showed that extensive oxide spallation occurred on the control samples but not on the GBE-treated samples. Oxide spallation is generally caused by stress generation in an oxide scale. There are generally two types of stresses in oxide scale: growth stress (also called intrinsic stress) developed during the oxidation process, and thermal stress developed on cooling due to the different thermal expansion between the oxide scale and the metal substrate. Although the origin of the growth stress is complex, it is strongly affected by the crystal structures, the oxide/metal volume ratio (also called Pilling–Bedworth ratio [18]), and the growth behavior of the oxide.

Since the austenite substrate has the same FCC structure as that of magnetite and spinel [19], and because magnetite and hematite have a similar Pilling–Bedworth ratio [20], the effect of crystal structure and volume of oxide and metal on growth stress is likely to be negligible. Therefore, for alloy 800H the growth stress is mainly affected by growth behavior of the oxide. To understand the growth behavior of the oxide, oxide texture was analyzed based on the EBSD data. Inverse pole figures (IPF) of magnetite and hematite on 3C and 4G samples, as shown in Fig. 7, were used as examples to show the oxide texture for the control and GBE-treated samples, respectively. According to the specimen layout during EBSD analysis, which is schematically shown in Fig. 6(c), the directions parallel to the oxide growth and oxide surface are

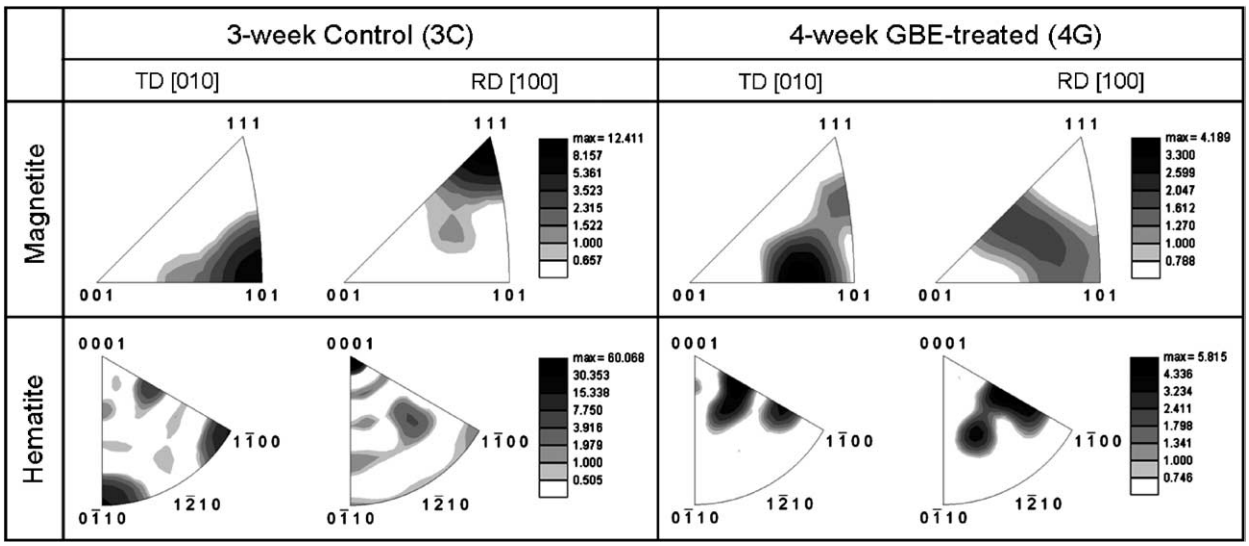

Fig. 7. Inverse pole figures (IPF) of magnetite and hematite in ~3-week SCW-exposed control (3C) and ~4-week SCW-exposed GBE-treated (4G) samples along the direction parallel to oxide growth (TD [010]) and oxide surface (RD [100]). The contrast of the IPFs indicates corresponding texture intensity scale as shown in the legend.

defined as TD [0 1 0] (transverse direction) and RD [1 0 0] (rolling direction), respectively. As shown in Fig. 7, both magnetite and hematite have texture on 3C and 4G samples along the TD [0 1 0] and RD [1 0 0] directions. However, the oxide texture intensity (defined as the ratio of measured intensity to the intensity of a random orientation) on the 3C sample is stronger than that on the 4G sample, as can be noted on the corresponding texture intensity scale bar.

The maximum texture intensities of magnetite and hematite on the 3C and 4G samples along the TD [0 1 0] and RD [1 0 0] directions are plotted in Fig. 8 for comparison. The control sample (3C) had stronger texture than the GBE-treated sample (4G), and the hematite texture was greater than the magnetite texture. For the 3C sample, the texture along the RD [1 0 0] direction was stronger than that along the TD [0 1 0] direction, especially for hematite texture in which the texture intensity along RD [1 0 0] direction was about three times of that along TD [0 1 0] direction. In contrast, the texture intensity along the RD [1 0 0] and TD [0 1 0] directions for the 4G sample was similar. These results indicate that the oxide formed in the 3C sample was more anisotropic than that in the GBE-treated 4G sample.

It has been reported that anisotropic energy of grain boundaries results in anisotropic texture development [21,22]. In addition, grain boundary energy is related to growth stress (intrinsic stress) [23]. It is suggested that the strong anisotropic oxide texture, especially that of hematite as shown in Fig. 8, developed on the control samples may anisotropically increase the growth stress and thus promote oxide scale cracking and spallation. GBE tunes the grain boundary character distribution, and thus the grain boundary energy distribution. Grain boundaries with relatively isotropic energy may be promoted after thermomechanical processing, which results in an oxide growth favoring improved spallation resistance. Therefore, the lower level of oxide spallation that occurred on the GBE-treated samples may be attributed to the relatively isotropic oxide texture. Moreover, the smaller hematite grain size on GBE-treated samples as shown in Fig. 6 could alleviate growth stress buildup [24] and thus benefit spallation resistance.

In addition to growth stress, thermal stress could be also alleviated in GBE-treated samples. This is because the thermal expansion of hematite is approximately a linear function of temperature, but the thermal expansion of magnetite is similar to that of hematite as a function of temperature up to ~300 °C and then increases with temperature [25]. The thermal expansion difference between hematite and magnetite at temperature above ~300 °C can be reduced by the higher hematite fraction in the oxide on GBE-treated samples.

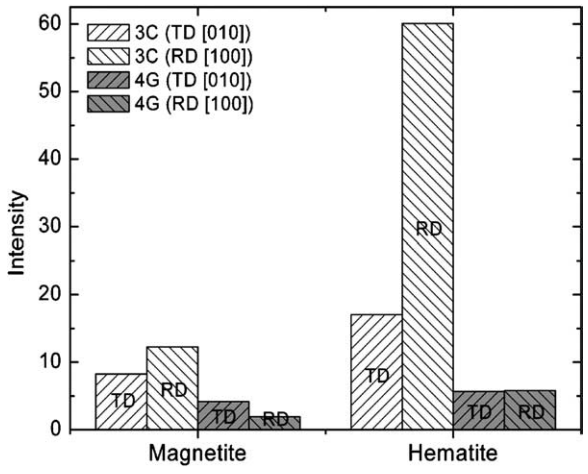

Fig. 8. Maximum texture intensity (defined as the ratio of measured to random orientation) of magnetite and hematite on 3-week SCW-exposed control (3C) and 4-week exposed GBE-treated (4G) samples along the direction parallel to oxide growth (TD [0 1 0]) and oxide surface (RD [1 0 0]).

4. Conclusion

Grain boundary engineering (GBE) was applied to INCOLOY alloy 800H by means of thermomechanical processing to improve protective oxidation behavior. Control (annealed) and GBE-treated alloy 800H samples were exposed in supercritical water with 25 ppb dissolved oxygen at 500 °C and 25 MPa. Experimental results indicate that extensive oxide spallation occurred on control samples but not on GBE-treated samples. A dual-layer structure of oxide scale formed on both control and GBE-treated samples with the outer layer composed of hematite and magnetite, and the inner layer composed of a mixture of austenite (substrate) and spinel. Relatively mild isotropic texture of oxide, smaller hematite grain size, larger hematite fraction in the oxide, and increased intermixing between the substrate and spinel were observed in GBE-treated samples by means of EBSD analyses. All of these features are believed to be beneficial for alleviating scale cracking and spallation. The

protective oxidation behavior of GBE-treated samples represented by the improved spallation resistance and slower oxidation rate is believed to be attributable to the highly increased population of low-Σ CSLBs.

Acknowledgements

The authors would like to thank M. Anderson, Y. Chen, J. Licht, and X. Ren, for their contribution to the supercritical water testing of the samples. This work is supported by the Idaho National Laboratory (INL) as part of the Department of Energy (DOE) Generation IV Initiative.

References

[1] T. Watanabe, Res. Mech. 11 (1984) 47.
[2] U. Erb, P. Lin, S. Kim, K.T. Aust, F. Gonzalez, G. Palumbo, Grain boundary engineering in nanocrystalline and polycrystalline materials, in: T.S. Srivatsan, R.A. Varin, (Eds.), Proceedings of the 10th International Symposium on Processing and Fabrication of Advanced Materials, Indianapolis, IN, USA, 5–8 November, 2001, p. 3.
[3] D.S. Lee, H.S. Ryoo, S.K. Hwang, Mat. Sci. Eng. A 354 (2003) 106.
[4] M. Shimada, H. Kokawa, Z.J. Wang, Y.S. Sato, I. Karibe, Acta Mater. 50 (2002) 2331.
[5] Y. Pan, B.L. Adams, T. Olson, N. Panayotou, Acta Mater. 44 (1996) 4685.
[6] V.Y. Gertsman, S.M. Bruemmer, Acta Mater. 49 (2001) 1589.
[7] V. Randle, The Role of the Coincidence Site Lattice in Grain Boundary Engineering, The Institute of Materials, London, 1996.
[8] Next generation nuclear plant materials research and development program plan, Idaho National Engineering and Environmental Laboratory, Bechtel BWXT Idaho, LLC, September, 2004, INEEL/EXT-04-02347.
[9] INCOLOY alloy 800H & 800HT, Technical Bulletin, Special Metals Publication SMC-047, March 2004. Available from: <http://www.specialmetals.com>.
[10] N. Otsuka, H. Fujikawa, Corrosion 47 (1991) 240.
[11] F.A. Khalid, N. Hussain, K.A. Shahid, Mat. Sci. Eng. A 265 (1999) 87.
[12] G.S. Was, T.R. Allen, Time, temperature, and dissolved oxygen dependence of oxidation of austenitic and ferritic–martensitic alloys in supercritical water, in: Proceedings of ICAPP '05, Seoul, Korea, 15–19 May, 2005.
[13] J. Armitt, D.R. Holmes, M.I. Manning, D.B. Meadowcroft, E. Metcalfe, The spalling of steam-grown oxide from superheater and reheater tube steels, EPRI Report FP 686, 1978.
[14] L. Tan, T.R. Allen, Mater. Met. Trans. A 36 (2005) 1921.
[15] D.P. Field, Ultramicroscopy 67 (1997) 1.
[16] L. Tan, Y. Yang, T.R. Allen, Corros. Sci., in press.
[17] T. Ericsson, Oxidation Metals 2 (1970) 173.
[18] N.B. Pilling, R.E. Bedworth, J. Inst. Metals 29 (1923) 529.
[19] The JCPDS Powder Diffraction File (PDF), International Centre for Diffraction Data (ICDD).
[20] P.R. Roberge, Handbook of Corrosion Engineering, McGraw-Hill, New York, 2000, p. 233.
[21] N.M. Hwang, B.J. Lee, C.H. Han, Scripta Mater. 37 (1997) 1761.
[22] N. Ma, A. Kazaryan, S.A. Dregia, Y. Wang, Acta Mater. 52 (2004) 3869.
[23] H. Sankur, W.J. Gunning, J.F. DeNatale, Appl. Optics 27 (1988) 1564.
[24] W. Gao, Z. Li, Mater. Res. 7 (2004) 175.
[25] Thermophysical Properties of Matter, Thermophysical Properties Research Center (TPRC), 1970.